Impact of F and S doping on $(Mn,Fe)_2(P,Si)$ giant magnetocaloric materials

Zhang, Fengqi; Batashev, Ivan; Shen, Qi; Wu, Ziying; Smith, Ronald I.; de Wijs, Gilles A.; van Dijk, Niels; Brück, Ekkes

DOI
10.1016/j.actamat.2022.118057

Publication date
2022

Document Version
Final published version

Published in
Acta Materialia

Acta Materialia 234 (2022) 118057

Contents lists available at ScienceDirect

Acta Materialia

journal homepage: www.elsevier.com/locate/actamat

Full length article

Impact of F and S doping on $(Mn,Fe)_2(P,Si)$ giant magnetocaloric materials

Fengqi Zhang[a,*], Ivan Batashev[a], Qi Shen[a], Ziying Wu[a], Ronald I. Smith[b], Gilles A. de Wijs[c], Niels van Dijk[a], Ekkes Brück[a]

[a] Fundamental Aspects of Materials and Energy (FAME), Faculty of Applied Sciences, Delft University of Technology, Delft, the Netherlands
[b] The ISIS Facility, STFC Rutherford Appleton Laboratory, Harwell Campus, Didcot, United Kingdom
[c] Radboud University, Institute for Molecules and Materials, Nijmegen, the Netherlands

ARTICLE INFO

Article history:
Received 24 February 2022
Revised 19 May 2022
Accepted 22 May 2022
Available online 24 May 2022

ABSTRACT

The quarternary $(Mn,Fe)_2(P,Si)$-based materials with a giant magnetocaloric effect (GMCE) at the ferromagnetic transition T_C are promising bulk materials for solid-state magnetic refrigeration. In the present study we demonstrate that doping with the light elements fluorine and sulfur can be used to adjust T_C near room temperature and tune the magnetocaloric properties. For F doping the first-order magnetic transition (FOMT) of $Mn_{0.60}Fe_{1.30}P_{0.64}Si_{0.36}F_x$ (x = 0.00, 0.01, 0.02, 0.03) is enhanced, which is explained by an enhanced magnetoelastic coupling. The magnetic entropy change $|\Delta S_m|$ at a field change ($\Delta\mu_0 H$) of 2 T markedly improved by 30% from 14.2 $Jkg^{-1}K^{-1}$ (x = 0.00) at 335 K to 20.2 $Jkg^{-1}K^{-1}$ (x = 0.03) at 297 K. For the F doped material the value of $|\Delta S_m|$ for $\Delta\mu_0 H$ = 1 T reaches 11.6 $Jkg^{-1}K^{-1}$ at 294 K, which is consistent with the calorimetric data (12.4 $Jkg^{-1}K^{-1}$). Neutron diffraction experiments reveal enhanced magnetic moments by F doping in agreement with the prediction of DFT calculation. For S doping in $Mn_{0.60}Fe_{1.25}P_{0.66-y}Si_{0.34}S_y$ (y = 0.00, 0.01, 0.02, 0.03, 0.04) three impurity phases have been found from microstructural analysis, which reduce the stability of the FOMT in the main phase and decrease T_C, e.g. the $|\Delta S_m|$ reduces from 7.9(12.6) $Jkg^{-1}K^{-1}$ (332 K) for the undoped sample to 3.4(6.2) $Jkg^{-1}K^{-1}$ (313 K) for the maximum doped sample for $\Delta\mu_0 H$ = 1(2) T. Neutron diffraction experiments combined with first-principles theoretical calculation, distinguish the occupation of F/S dopants and the tuning mechanism for light element doping, corresponding to subtle structural changes and a strengthening of the covalent bonding between metal and metalloid atoms. It is found that the light elements F and S can effectively regulate the magnetocaloric properties and provide fundamental understanding of $(Mn,Fe)_2(P,Si)$-based intermetallic compounds.

1. Introduction

The giant magnetocaloric effect (GMCE), accompanied by an isothermal magnetic entropy change (ΔS_m) and an adiabatic temperature change (ΔT_{ad}), enables several promising applications in the form of: (*i*) magnetic refrigeration [1], (*ii*) magnetic heat pumps [2] and (*iii*) thermomagnetic motors and generators to covert low-temperature waste heat into electricity [3,4]. In the last two decades, numerous first-order magnetic transition (FOMT) magnetocaloric materials (MCMs) that demonstrate a GMCE have sprung up, including $Gd_5(Si_2Ge_2)$ [5], $(Mn,Fe)_2(P,X)$-based compounds (X = As, Ge, Si) [6], $La(Fe,Si)_{13}$-based materials [7], Ni-Mn-X based magnetic Heusler alloys (X = Ga, In, Sn, Sb) [8], FeRh [9], Mn_2Sb based alloys [10] and Mn-M-X (M = Co, Ni and X = Si, Ge) alloys [11]. Within these MCMs the $(Mn,Fe)_2(P,Si)$-based alloys with a hexagonal crystal structure have attracted considerable attention because they are rare-earth free, have no toxic elements, are low cost and have a tunable Curie temperature (T_C). This materials system demonstrates a strong magnetoelastic coupling controlled by the magnetic, structural and electronic degrees of freedom.

Different strategies have been proposed to further optimize the GMCE performance, for example engineering chemical pressure (by atom substitution or interstitial doping), applying hydrostatic pressure or multiple mechanical stimuli (multicaloric effect) [12,13]. Doping with light elements (e.g. H, B, C, N) can be an effective method to tailor the magnetic properties. For example, in another prototypical magnetoelastic MCM system $La(Fe,Si)_{13}$ the insertion of H (as well as B and C) atoms significantly increases T_C

* Corresponding author.
E-mail address: F.Zhang-7@tudelft.nl (F. Zhang).

https://doi.org/10.1016/j.actamat.2022.118057

[14]. For NiMn-based Heusler alloys substitutional B or interstitial C are both helpful to adjust the magnetostructural phase transition [15–18]. Specifically for $(Mn,Fe)_2(P,Si)$-based materials B/C/N atoms present positive effects. For example, substitution of B (up to 7.5%) in $MnFe_{0.95}P_{0.595}B_{0.075}Si_{0.33}$ can dramatically reduce the thermal hysteresis (ΔT_{hys}) from 75 K to only 1.6 K, and thereby effectively improve the reversibility of the GMCE [19]. Compared to doping with metal elements (e.g. V, Ni, Co, Zr, Nb, Mo) [20–23], the doping with light elements provides a unique platform to investigate the nature of the magnetoelastic isostructural transition for this metal-metalloid system [24]. In addition to the B/C/N doping of $(Mn,Fe)_2(P,Si)$-based MCMs, doping with F and S, which have high electronegativity values of $\chi_F \approx 4.0$ and 2.5, respectively [25], enables a systematic exploration on the question of how light elements influence the fundamental magnetic properties. It is noteworthy that, from the classical Pauling's scale [26,27], the element F ($\chi_F \approx 4$) possesses the highest electronegativity value [25] which can help us understand the role of the electrons within $(Mn,Fe)_2(P,Si)$-based MCMs, especially in comparison with other light elements like B. Additionally, S the neighboring element of P, is rarely reported for MCMs and the increase in electronegativity from P ($\chi_F \approx 2.1$) to S ($\chi_F \approx 2.5$) can be considered dominant. For S the influence of the chemical pressure is expected to be limited as the atomic radius is very similar for P (r = 1.07 Å) and for S (r = 1.05 Å) [28]. These properties inspire and further motivate us to investigate the effects of F and S doping for $(Mn,Fe)_2(P,Si)$-based MCMs.

In the present study, the F and S doped $Mn_{0.60}Fe_{1.30}P_{0.64}Si_{0.36}F_x$ (x = 0.00, 0.01, 0.02, 0.03) and $Mn_{0.60}Fe_{1.25}P_{0.66-y}Si_{0.34}S_y$ (y = 0.00, 0.01, 0.02, 0.03, 0.04) alloys have successfully been produced. Here the thermodynamic, MCE and structural information is reported. It is found that F-doped materials show improved magnetic moments and GMCE performance. The increase in moments is in agreement with Density Functional Theory (DFT) calculations. Additional neutron diffraction (ND) experiments reveal that the MCE properties can be tuned by controlling the atomic distances among different metal-metal or metal-metalloid atom pairs. Electron Localization Function (ELF) calculations clarify that subtle changes in atomic distances as well as the covalent bonding, defined by the *p-d* hybridization, jointly control the GMCE properties of the $(Mn,Fe)_2(P,Si)$-based materials. Our current study illuminates how light elements affect the magnetoelastic coupling and the GMCE in metal-metalloid MCMs.

2. Experimental and computational procedures

The off-stoichiometric bulk $Mn_{0.60}Fe_{1.30}P_{0.64}Si_{0.36}F_x$ (x = 0.00, 0.01, 0.02, 0.03) and $Mn_{0.60}Fe_{1.25}P_{0.66-y}Si_{0.34}S_y$ (y = 0.00, 0.01, 0.02, 0.03, 0.04) MCMs were synthesized by solid-state chemical reaction [20]. Mn (99.9%), Fe (99.9%), red-P (99.7%), Si (99.9%), FeF_3 (97.0%) and FeS_2 (99.8%) powders with a total mass of 10 g were mixed and milled for 10 h at 380 rpm. The pressed cylindrical tablets were sealed in quartz tubes under 200 mbar Ar atmosphere and annealed for 25 h at 1373 K. Subsequently, these samples were rapidly quenched in cold water, followed by a pre-cooling process in liquid nitrogen to remove the so-called "virgin effect" [29]. Note that the ratio between metallic (Mn,Fe) and non-metallic (P,Si) in the nominal composition of the studied alloys has been chosen to deviate from 2:1 in order to achieve the smallest amount of impurity phases [30].

Differential scanning calorimetry (DSC) measurements were carried out using a commercial TA-Q2000 DSC calorimeter. The DSC measurements under different magnetic fields were performed in a home-built Peltier cell-based DSC, where the calorimetric ΔS_m and ΔT_{ad} were derived from specific heat measurements [31]. X-ray diffraction (XRD) patterns were collected using an Anton Paar TTK450 temperature-tunable sample chamber and a PANalytical X-pert Pro diffractometer with Cu K_α radiation. Neutron diffraction (ND) experiments were performed on the Polaris time-of-flight powder diffractometer at the ISIS pulsed spallation neutron source (UK). About 6 g of powder sample was placed into a vanadium can (8 mm diameter) and neutron diffraction data were collected at room temperature (RT). Instrumental details can be found in ref. [32,33]. The XRD and neutron patterns were analyzed using Fullprof's implementation of the Rietveld refinement method [34]. Temperature-dependent magnetization (*M-T*) and field-dependent magnetization (*M-H*) curves were measured in a superconducting quantum interference device (SQUID, Quantum Design MPMS 5XL) magnetometer. Scanning electron microscopy (SEM) was carried out on a JSM-7500F Field Emission Scanning Electron Microscope to study the morphology and composition.

First-principles calculations in the framework of the density functional theory (DFT) were performed using the Vienna *ab* initio simulation package (VASP) [35,36]. The projector augmented wave (PAW) method [37,38] was used with the generalized gradient approximation of Perdew-Burke-Ernzerhof [39] for the exchange correlation functional. Elastic constants are calculated by applying appropriate cell-volume conserving deformations [40–42]. In all calculations the following electrons were treated as valence electrons: 3*p*, 4*s*, 3*d* for Mn; 4*s* and 3*d* for Fe; 3*s* and 3*p* for P, Si and S; 2*s* and 2*p* for F. A 2 × 2 × 2 supercell based on a 9-atom unit cell with the composition $Mn_{0.5}Fe_{1.5}P_{0.67}Si_{0.33}$ was used in the calculations. All *3f* sites were filled by Fe atoms while 3*g* sites were semi-randomly occupied by Fe and Mn atoms. Si atoms were inserted at the *1b* site and P atoms at the *2c* site in order to avoid the computational cost related to larger supercells to account for the positional disorder [42]. The structure was fully relaxed on a gamma-centered ***k***-grid of 7 × 7 × 11 with the 2nd order Methfessel-Paxton method [43] and a smearing width of 0.05 eV. A smaller 1 × 1 × 2 supercell with a ***k***-grid of 14 × 14 × 11 was used for calculations of the electron localization function. The kinetic energy cutoff was set at 500 eV, the force convergence tolerance was set to 0.1 meV/Å and the energies were converged to 1 μeV.

To determine the F and S site preference, the formation energies of the structures with dopants placed on all possible crystallographic sites were compared. The energy cost of forming each structure is calculated as the difference between the energies of doped (E_{doped}) and pure (E_{pure}) compounds minus the chemical potential of the dopant (μ_d) plus the chemical potential of the atom replaced by the dopant (μ_s):

$$E_f = E_{doped} + \mu_s - (E_{pure} + \mu_d) \quad (1)$$

Chemical potentials were calculated by first optimizing bcc iron, alpha manganese, diamond cubic silicon, orthorhombic sulfur and tetrahedral phosphorus and then using the resulting total energies per atom. For fluorine chemical potential was obtained from the total energy of the isolated F_2 molecule. To investigate the type of the chemical bonds the electron localization function (ELF) [44] was analyzed. The ELF allows for an accurate characterization of the bond nature based on the electron densities. This characterization is based on a topological analysis of local quantum-mechanical functions related to the Pauli exclusion principle. The ELF represents the possibility of finding a second electron with the same spin in the vicinity of the reference electron. Higher ELF values correspond to areas with more localized electrons and indicate a stronger covalent bonding.

3. Results

The specific heat as a function of temperature (measured by zero-field DSC) for the $Mn_{0.60}Fe_{1.30}P_{0.64}Si_{0.36}F_x$ (x = 0.00, 0.01, 0.02, 0.03) materials is presented in Fig. 1a. It is observed endothermic

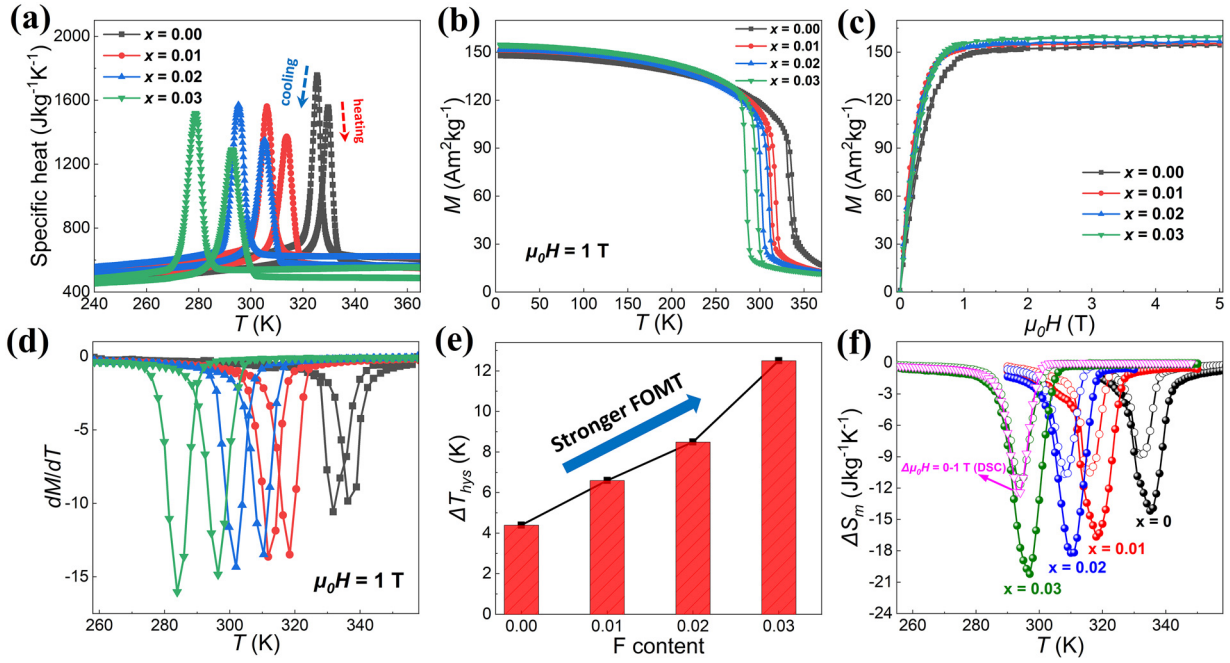

Fig. 1. (a) Specific heat derived from DSC experiments for $Mn_{0.60}Fe_{1.30}P_{0.64}Si_{0.36}F_x$ (x = 0.00, 0.01, 0.02, 0.03) materials upon heating and cooling. (b) Isofield M-T curves for $Mn_{0.60}Fe_{1.30}P_{0.64}Si_{0.36}F_x$ (x = 0.00, 0.01, 0.02, 0.03) alloys in an applied field of 1 T. (c) Corresponding isothermal M-H curves as a function of applied field at 5 K. (d) Temperature dependence of dM/dT derived from the M-T curves. (e) ΔT_{hys} change for different F-doped materials. (f) ΔS_m change for a field change ($\Delta\mu_0 H$) of 1 T (open symbols) and 2 T (solid symbols) at different F contents. Note that the magenta curve is extracted from DSC under an applied field change of 1 T.

Table 1
Summary of the Curie temperature upon cooling (T_C-cooling) and heating (T_C-heating), the thermal hysteresis ΔT_{hys}, the latent heat L and total entropy change (ΔS_{tot}) for $Mn_{0.60}Fe_{1.30}P_{0.64}Si_{0.36}F_x$ (x = 0.00, 0.01, 0.02, 0.03) materials, measured in DSC and SQUID.

Sample	Tc-cooling DSC (K)	Tc-cooling SQUID (K)	Tc-heating DSC (K)	Tc-heating SQUID (K)	ΔT_{hys} DSC (K)	ΔT_{hys} SQUID (K)	L (J/g)	$\lvert\Delta S_{tot}\rvert$ (Jkg^{-1}K^{-1})
x = 0.00	325.4	331.8	329.7	336.2	4.3	4.4	4.8	14.8
x = 0.01	306.8	311.8	313.9	318.4	7.1	6.6	5.1	16.6
x = 0.02	295.3	301.9	305.2	310.4	9.9	8.5	5.4	18.3
x = 0.03	278.8	283.9	292.8	296.4	14.0	12.5	6.0	21.7

and exothermic peaks shift to lower temperatures with increasing F dopant content. The latent heat (L) of the phase transition has been estimated by $L = \int_{T_s}^{T_f} \frac{dQ}{dT} dT$, where dQ/dT is the change in heat flow with respect to temperature, and T_s and T_f are the start and end temperatures [45]. The entropy change at T_C corresponds to $\Delta S_{tot} = L/T_C$. The main thermodynamic parameters extracted from the DSC measurements are summarized in Table 1.

The M-T curves at 1 T for the $Mn_{0.60}Fe_{1.30}P_{0.64}Si_{0.36}F_x$ (x = 0.00, 0.01, 0.02, 0.03) materials are shown in Fig. 1b. A giant FOMT from strong ferromagnetism at low temperature to paramagnetism at high temperature is observed with phase transitions near room temperature. $(Mn,Fe)_2(P,Si)$-based alloys are found to be sensitive to F doping with a sensitivity of the phase transition of $dT_C/dx = -13.3$ K/$at.$% F. In addition to the shift in T_C, two striking phenomena for F doping are found (i) a weak enhancement of the saturation magnetization and (ii) an enhancement of the FOMT. Furthermore, as shown in Fig. 1e, the thermal hysteresis ΔT_{hys} continuously increases from 4.4 K (x = 0.00) to 12.5 K (x = 0.03), which is in line with the enhanced FOMT indicated in Fig. 1f.

These findings are unusual as most doping elements in $(Mn,Fe)_2(P,Si)$-based alloys result in a decrease in saturation magnetization and a lower thermal hysteresis. In particular, it has been reported previously that B doping significantly reduces ΔT_{hys}, resulting in an excellent cyclic adiabatic temperature change (ΔT_{cyclic} = 2.8 K under $\Delta\mu_0 H$ = 1.1 T) [19]. Considering the difference in free electrons among B ($2s^2 2p^1$) and F ($2s^2 2p^5$) and the strong electronegativity ($\chi_F \approx 4.0$) for F [25], the competition between covalent bonding and ferromagnetic exchange coupling [24] is expected to be responsible to the difference in magnetic response for these doping elements.

As shown in Fig. 1d the value of T_C has been determined from the minimum in dM/dT and is collected in Table 1 for comparison to DSC data. The value of ΔS_m for the $Mn_{0.60}Fe_{1.30}P_{0.64}Si_{0.36}F_x$ (x = 0.00, 0.01, 0.02, 0.03) samples, defined as the entropy change caused by a magnetic field change, has been obtained from the M-T curves in field and is shown in Fig. 1f. The maximum value of $|\Delta S_m|$ for $\Delta\mu_0 H$ = 2 T shows a significant improvement of 30% from 14.2 Jkg^{-1}K^{-1} at 335 K for the undoped sample (x = 0.00) to 20.2 Jkg^{-1}K^{-1} at 297 K for the highest doped sample (x = 0.03). For a field change of $\mu_0 H$ = 1 T the entropy change $|\Delta S_m|$ reaches 11.6 Jkg^{-1}K^{-1} at 294 K for the x = 0.03 sample, which is consistent with the in-field DSC data (12.4 Jkg^{-1}K^{-1}). These values are higher than the values for the archetypical MCM Gd of 2.8 (5.2) Jkg^{-1}K^{-1} with $\Delta\mu_0 H$ = 1(2) T [46]. Fig. S1a and S1b (Supporting Information) illustrate the conventional MCE upon applying magnetic fields. The adiabatic temperature change for the x = 0.03 sample is extracted from calorimetric measurements in Fig. S1c (Supporting Information) and reaches ΔT_{ad} = 2.2(3.9) K with $\Delta\mu_0 H$ = 1(1.5) T, which is competitive with other MCMs [47].

Similar to F doping discussed above also S doping can be considered. In Fig. 2a the specific heat upon heating and cooling is shown for $Mn_{0.60}Fe_{1.25}P_{0.66-y}Si_{0.34}S_y$ (y = 0.00, 0.01, 0.02, 0.03, 0.04) samples. For all samples a FOMT is observed. For increas-

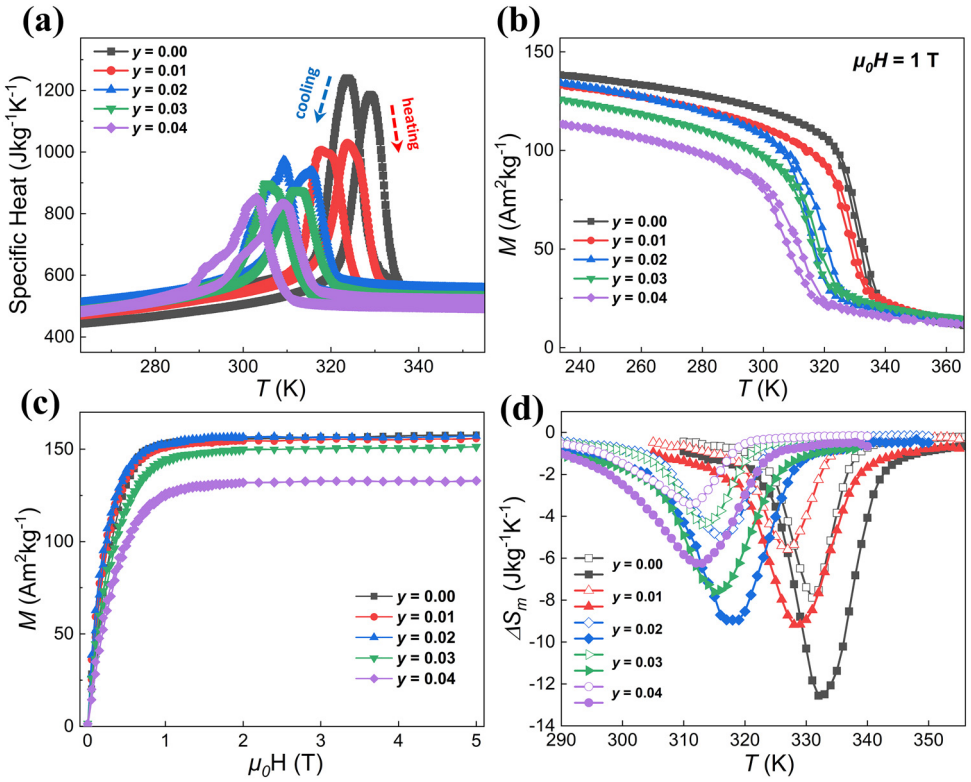

Fig. 2. (a) Specific heat derived from DSC experiments for $Mn_{0.60}Fe_{1.25}P_{0.66-y}Si_{0.34}S_y$ (y = 0.00, 0.01, 0.02, 0.03, 0.04) materials upon heating and cooling. (b) Isofield M-T curves for $Mn_{0.60}Fe_{1.25}P_{0.66-y}Si_{0.34}S_y$ (y = 0.00, 0.01, 0.02, 0.03, 0.04) materials under 1 T. (c) Corresponding isothermal M-H curves at 5 K. (d) Entropy change ΔS_m for $\Delta\mu_0 H$ = 1 T (open symbols) and 2 T (solid symbols) as a function of different S doping contents.

Table 2
Summary of T_C-cooling, T_C-heating, ΔT_{hys}, L and ΔS_{tot} for $Mn_{0.60}Fe_{1.25}P_{0.66-y}Si_{0.34}S_y$ (y = 0.00, 0.01, 0.02, 0.03, 0.04) materials, measured in DSC and SQUID.

Sample	*Tc*-cooling DSC (K)	*Tc*-cooling SQUID (K)	*Tc*-heating DSC (K)	*Tc*-heating SQUID (K)	ΔT_{hys} DSC (K)	ΔT_{hys} SQUID (K)	L (J/g)	$\lvert\Delta S_{tot}\rvert$ ($Jkg^{-1}K^{-1}$)
y = 0.00	323.9	325.3	329.2	331.6	5.3	6.3	4.9	15.2
y = 0.01	319.9	323.2	325.8	328.0	5.7	4.8	4.2	13.2
y = 0.02	309.7	315.2	315.8	319.3	6.1	4.1	3.8	12.2
y = 0.03	305.6	308.8	312.2	316.1	6.6	7.3	3.6	11.7
y = 0.04	303.1	305.9	309.2	313.0	6.1	7.1	3.0	9.9

ing S doping T_C shifts to lower temperature, ΔT_{hys} remains almost constant, while L and $|\Delta S_{tot}|$ continuously decreases, which indicates a weakening of the FOMT, as illustrated in Table 2. Fig. 2b shows the M-T curves for the S-doped samples in an applied field of 1 T. By varying the S content, the T_C upon heating shifts from 332 K for the undoped sample (y = 0.00) to 313 K for the highest doped sample (y = 0.04). The effect of S doping on T_C is only dT_C/dy = −4.8 K/*at.*% S, which is significantly weaker than that of F doping with dT_C/dx = −13.3 K/*at.*% F. Fig. 2c demonstrates the corresponding M-H curves at 5 K. M_S slightly decreases from y = 0.00 to y = 0.03, with a more rapid decline between y = 0.03 (151.5 Am^2kg^{-1}) and y = 0.04 (132.8 Am^2kg^{-1}). Fig. 2d shows that $|\Delta S_m|$ gradually decreases with increasing S doping. The entropy change $|\Delta S_m|$ reduces from 7.9(12.6) $Jkg^{-1}K^{-1}$ for the undoped sample (y = 0) to 3.4(6.2) $Jkg^{-1}K^{-1}$ for the highest doped sample (y = 0.04) in a field change of $\Delta\mu_0 H$ = 1(2) T.

To further investigate the mechanism responsible for the weakening of the FOMT in $Mn_{0.60}Fe_{1.25}P_{0.66-y}Si_{0.34}S_y$ (y = 0.00, 0.01, 0.02, 0.03, 0.04) materials SEM measurements are applied. Fig. 3a shows the backscattered electrons (BSE) SEM image from the $Mn_{0.60}Fe_{1.25}P_{0.63}Si_{0.34}S_{0.03}$ sample, revealing three distinct impurities randomly distributed within the main phase matrix. The composition of these three types of impurities are determined as $Mn_{47.8}Fe_{8.3}P_{2.4}Si_{6.2}S_{35.3}$ (impurity 1: MnS-based), $Mn_{17.3}Fe_{19.8}P_{4.9}Si_{49.6}S_{8.4}$ (impurity 2: (Mn,Fe)Si-based) and $Mn_{20.5}Fe_{40.0}P_{14.7}Si_{24.0}S_{0.8}$ (impurity 3: $(Mn,Fe)_3Si$-based), respectively. Interestingly, besides the MnS-based and $(Mn,Fe)_3Si$-based impurities also observed by X-ray diffraction, another (Mn,Fe)Si-based impurity has been found in $(Mn,Fe)_2(P,Si)$-based MCMs [48]. The reason for the appearance of this (Mn,Fe)Si-based impurity could be the decomposition of $(Mn,Fe)_5Si_3$ below 800 °C into $(Mn,Fe)_3Si$ and (Mn,Fe)Si [49,50]. These closely arranged impurities within matrix might also be attributed to compositional fluctuations in the main phase, which may explain the appearance of shoulders in some of the specific heat measurement peaks in Fig. 2a. Additionally, the corresponding composition line-scan profile in Fig. 3b clearly illustrates the competition among (Mn,Fe)Si-based and MnS-based impurities.

In comparison to X-ray diffraction, neutron diffraction (ND) often possesses a higher sensitivity to light elements (e.g. H, B, C, N, O, F, S), therefore it has been successfully employed to resolve the occupation of B, C and N dopants within the $(Mn,Fe)_2(P,Si)$-based lattice structure [51,52]. Due to the neutron spin ND is sensitive to both the lattice structure and the magnetic structure [53,54]. Here, we present the crystal structures at RT for $Mn_{0.60}Fe_{1.30}P_{0.64}Si_{0.36}F_x$ (x = 0.00, 0.02) and $Mn_{0.60}Fe_{1.25}P_{0.66-y}Si_{0.34}S_y$ (y = 0.00, 0.02) refined from our ND data, Fig. 4(a,b) and (c,d), respectively. Good fits to the data were obtained using a hexagonal unit cell (space group

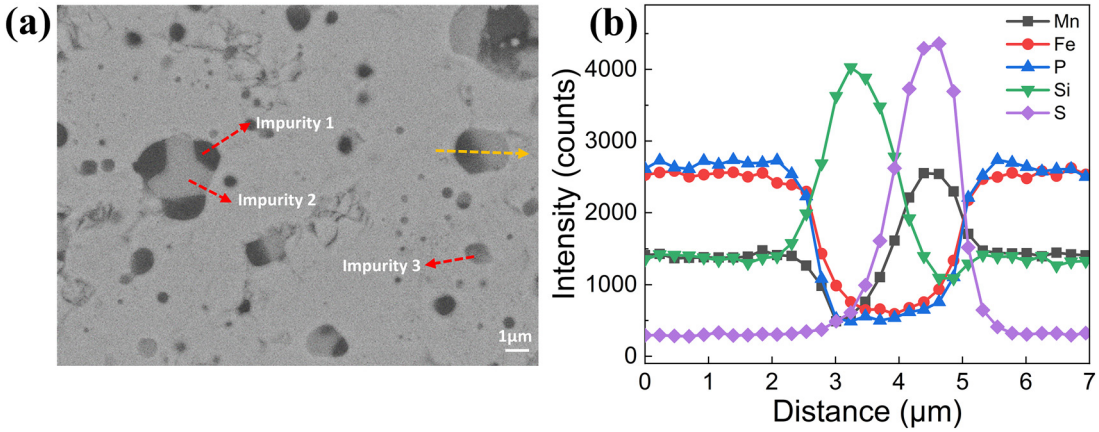

Fig. 3. (a) Backscattered electron SEM image for the $Mn_{0.60}Fe_{1.25}P_{0.63}Si_{0.34}S_{0.03}$ alloy. (b) Corresponding composition line-scan profile along the yellow dashed line in (a).

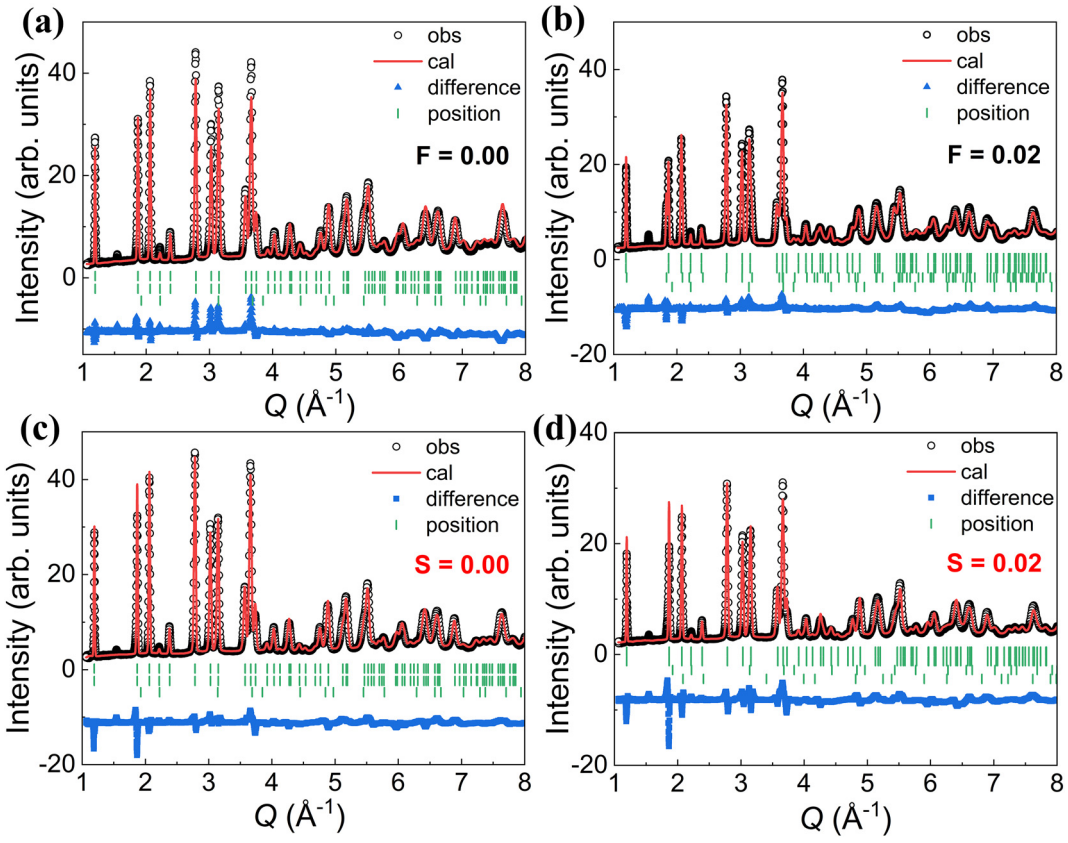

Fig. 4. Fitted powder neutron diffraction patterns for Fe-rich (a) $Mn_{0.60}Fe_{1.30}P_{0.64}Si_{0.36}F_{0.00}$, (b) $Mn_{0.60}Fe_{1.30}P_{0.64}Si_{0.36}F_{0.02}$, (c) $Mn_{0.60}Fe_{1.25}P_{0.66}Si_{0.34}S_{0.00}$ and (d) $Mn_{0.60}Fe_{1.25}P_{0.64}Si_{0.34}S_{0.02}$ collected in the Polaris detector bank 3 ($<2\theta> \approx 40.4 - 66.4°$) at RT as a function of the wave vector transfer *Q*. Black circles indicate the observed data points, red lines the calculated profile, blue lines the difference and vertical lines the Bragg peak positions.

P-62*m*) with both Mn and Fe magnetic moments aligned parallel to the *c* axis. The orientation of the magnetic moments is different from previous studies of Mn-rich samples, where the moments were found to be oriented in the *a*-*b* plane [55]. The magnetic moments for Fe-rich samples are preferentially aligned along *c* axis, in a similar manner to its parent Fe_2P counterpart [56,57]. This indicates that the direction of moments is strongly determined by the Mn/Fe ratio in $(Mn,Fe)_2(P,Si)$-based materials. The fitted ND patterns for all F-doped and S-doped samples are exhibited in Figs.S2 and S3, respectively (Supporting Information). The structural parameters (including the XRD data for comparison) and the magnetic moments derived from Rietveld refinement can be found in Tables S1 and S2 (Supporting Information).

The lattice parameters *a* and *c* of the hexagonal Fe_2P type lattice structure for the F-doped and S-doped alloys, derived from the ND experiments, are shown in Fig. 5a,b. Fig. 5a shows that at RT the lattice parameters exhibit discontinuous changes in *a* and *c* depending on their magnetic state (ferromagnetic (FM)/Coexistence/paramagnetic (PM)) with anomalies in $\Delta a/a$ ($\Delta c/c$) of the order of −0.91% (+1.73%), while lattice symmetry is conserved in different magnetic states. As shown in Fig. 5c, combining the ND data with high-temperature PM X-ray data, one can easily distinguish the difference in *c*/*a* ratio among the FM state, two-phase coexistence and the PM state. The change in *c*/*a* ratio is closely related to the magnetic exchange interactions that control the magnetoelastic coupling in these materials [58].

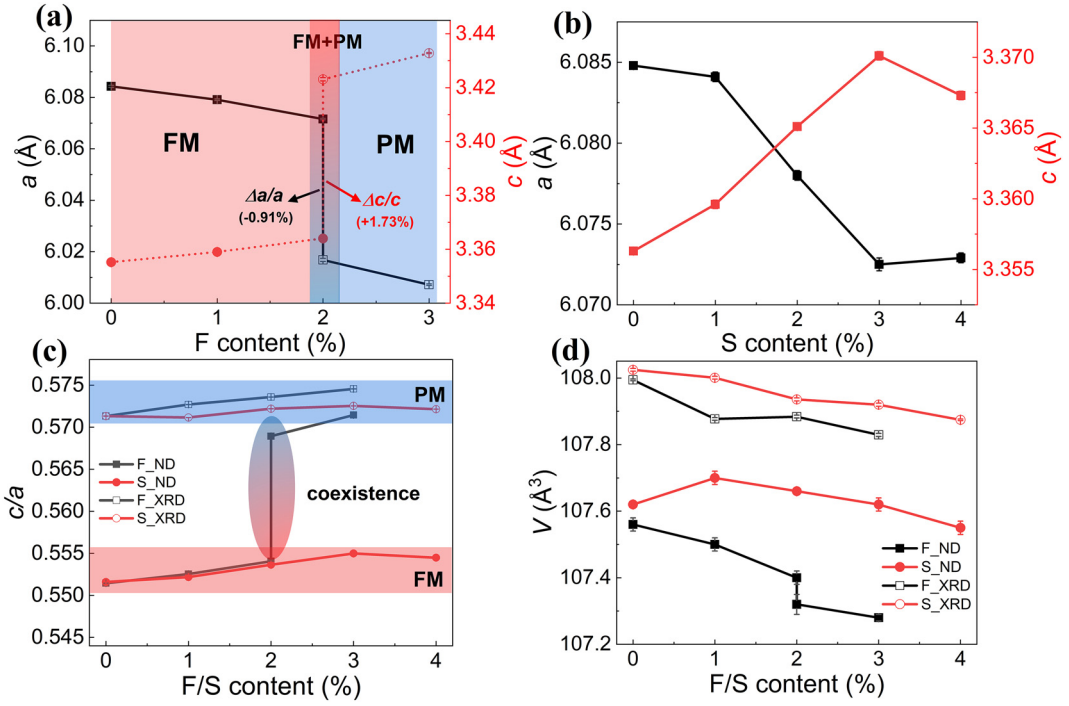

Fig. 5. Lattice parameters a and c as a function of the F and S doping concentration for the (a) $Mn_{0.60}Fe_{1.30}P_{0.64}Si_{0.36}F_x$ (x = 0.00, 0.01, 0.02, 0.03) and (b) $Mn_{0.60}Fe_{1.25}P_{0.66\text{-}y}Si_{0.34}S_y$ (y = 0.00, 0.01, 0.02, 0.03, 0.04) alloys. Note that the F-doped samples have different magnetic states (FM, PM, phase coexistence), while the S-doped samples are all in the FM state. (c) c/a ratio and (d) unit-cell volume V as a function of the F/S doping concentration. Note that solid symbols correspond to ND data and open symbols to XRD data, respectively.

In Fig. 5c the magnitude of the jump in c/a ratio for the F-doped sample with x = 0.02 is about 2.6%, corresponding to a relatively low ΔT_{hys} of 9 K. Moreover, the cell volume V for the F-doped and S-doped samples derived from the ND and XRD data are presented in Fig. 5d. The slight differences are caused by the thermal expansion of different experiment temperatures (ND at RT and XRD at T_C + 100 K).

A comparison of the present data with those from Miao et al. [52] for B, C, N-doped $(Mn,Fe)_2(P,Si)$-based materials and with DFT calculations, makes it possible to further investigate the effect of doping (interstitial/substitutional) and site occupancy of F/S atoms. As demonstrated in Fig. 6a, compared with C doping (red curve; interstitial site), F (green curve) and S (purple curve) atoms enter the structure as substitutional atoms because the covalent radius of F (0.57 Å) and S (1.05 Å), as well as B (0.84 Å), are smaller than the non-metal elements P (1.07 Å) and Si (1.11 Å) within the $(Mn,Fe)_2(P,Si)$ structure [28], which leads to the decrease in normalized cell volume. The decrease in V for S is distinctly lower than that for F, which could be ascribed to the comparable atom radius among S, P and Si. In addition, based on our neutron diffraction results, accurate preferred sites for the F and S atoms have been obtained: F preferentially occupies the *1b* site, while S preferentially occupies the *2c* site with no evidence found for any preferential occupancy of the P and Si atoms on these sites. This preference is illustrated in the schematic representation in Fig. 6b and matches the conclusions for doped Fe_2P [51]. According to DFT calculations, the formation energies E_f of various site occupation models for these two systems confirm the experimentally obtained preferred sites, as shown in Fig. S6 (Supporting Information).

4. Discussion

One interesting phenomenon about F doping is the surprisingly continuous enhancement of the MCE accompanied by an increase in thermal hysteresis. The thermal hysteresis is closely associated with the energy barrier for nucleation during the FOMT [59]. Different strategies to minimize the hysteresis have been proposed. For magnetostructural MCMs improving the structural compatibility between both phases is recommended [11,60], while metal-element doping or introducing secondary phases are effective for $(Mn,Fe)_2(P,Si)$-type and $La(Fe,Si)_{13}$-type magnetoelastic MCMs [22,23,61]. The magnetoelastic transition is sensitive to the transition-induced elastic strain energy (U_E) because of the lattice mismatch between the PM and FM phases (no symmetry change) [42,62]. U_E in a hexagonal system [63–65] can be estimated by the formula:

$$U_E = (C_{11} + C_{12})e_1^2 + 2C_{13}e_1e_3 + \frac{1}{2}C_{33}e_3^2 \quad (2)$$

where the C_{ij} (i, j = 1,2,3,4,5,6) are the elastic constants (calculated with DFT, see Section. 2) and $e_{i,j}$ are the elastic strains ($e_1 = e_2 = \Delta a/a$ and $e_3 = \Delta c/c$ in an hexagonal system) [23,42]. Consequently, the corresponding U_E for the $Mn_{0.60}Fe_{1.30}P_{0.64}Si_{0.36}F_{0.02}$ sample (ΔT_{hys} = 8.5 K) is estimated to be 7.8 kJ/mol. The U_E for the parent $Mn_{0.60}Fe_{1.30}P_{0.64}Si_{0.36}$ sample (ΔT_{hys} = 4.4 K) is only around 4.1 kJ/mol (derived from temperature-dependent XRD at T_C). Therefore, the increase in ΔT_{hys} for F doping is correlated with the enhanced elastic transition energy.

Additionally, Arrott plots ($\mu_0 H/M$ versus M^2) for F-doped and S-doped samples present in Figs. S7 and S8 (Supporting Information) were constructed to further analyze the nature of the transition. According to the Banerjee criterion [66] a clear FOMT feature is found for all samples because of the "S-shaped" curves, which confirms the other FOMT features (thermal hysteresis, peak in the specific heat and lattice discontinuities at the transition).

The magnetic moments for the Fe and Mn atoms as well as the total moment per formula unit for our $Mn_{0.60}Fe_{1.30}P_{0.64}Si_{0.36}F_x$ (x = 0.00, 0.01, 0.02) and $Mn_{0.60}Fe_{1.25}P_{0.66\text{-}y}Si_{0.34}S_y$ (y = 0.00,0.01, 0.02, 0.03, 0.04) alloys were determined from the neutron diffrac-

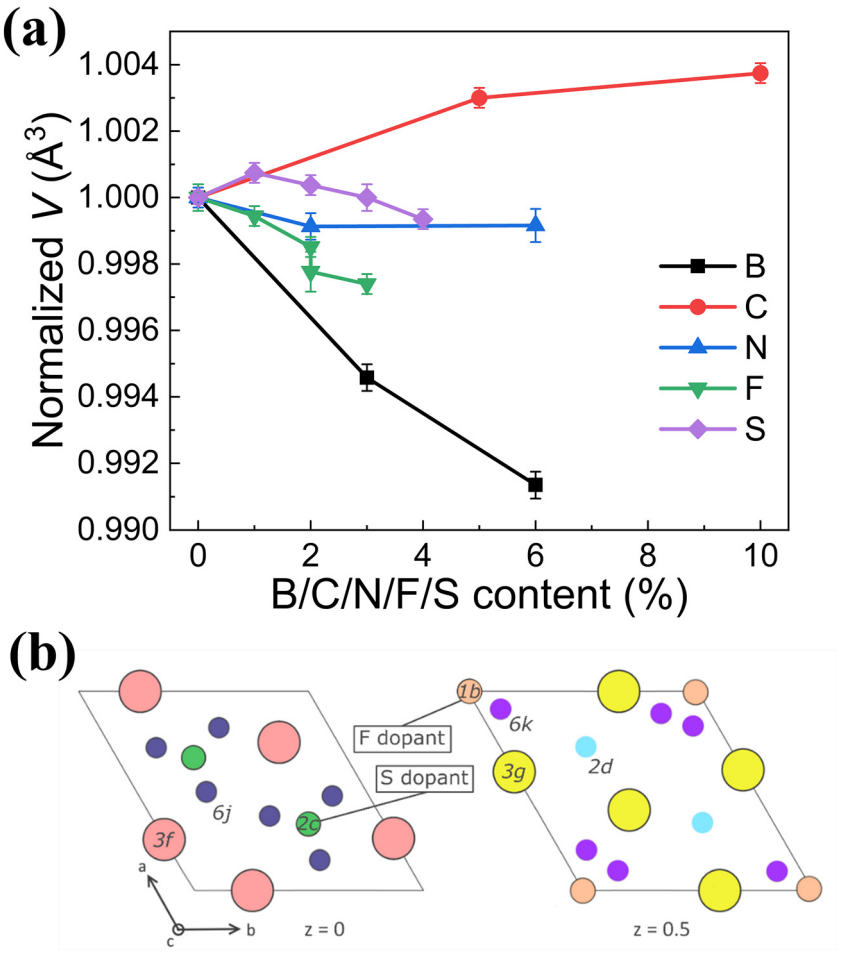

Fig. 6. (a) Normalized volume as a function of the B, C, N, F and S doping concentration, obtained from ND data. (b) Schematic representation of $(Mn,Fe)_2(P,Si)$-type lattice structure and the corresponding potential atom positions of the F/S dopant in the basal plane at $z = 0$ and $z = 0.5$.

tion data by magnetic structure refinement and are shown in Fig. 7(a,b). It shows that Mn(3*g*) atoms are responsible for the main magnetic moments, and that the Mn moments almost remain constant, while the Fe(3*f*) moments significantly decrease, especially near to the transition region (see the F-doped sample with $x = 0.02$ and the S-doped sample with $y = 0.04$). The so-called "mixed magnetism" [67] in the $(Mn,Fe)_2(P,Si)$ system was applied to explain that, compared with the robustness of Mn(3*g*) moments, the Fe(3*f*) moments are relatively sensitive to the phase transition reflected in the "Fe moment quenching" phenomenon, which has been demonstrated in theoretical calculations [67,68]. The Fe(3*f*) intralayer coupling is easily influenced by external stimuli like chemical pressure (e.g. by heteroatomic doping), hence in the next section we will further investigate these atomic-scale variations among different doping systems. The total magnetic moments obtained from macroscopic magnetization measurements at RT are in good agreement with the neutron diffraction results at the same temperature. Interestingly, in comparison to the experimental results (red curve), the DFT calculations for the total moment (black curve) also confirm that F doping (in contrast with other elements) promotes a moment enhancement. This significant enhancement is ascribed to the increase in Fe moment, while the Mn moments maintain constant, as shown in Fig. 7c. For S-doping Fig. 7d shows that even though the moment hardly changes in the theoretical calculations, the magnetic moment from magnetization measurements show a decrease, which could be caused by the introduction of Mn-based secondary phases as DFT calculations didn't consider this effect, and a sudden increase in the amount of (Mn,Fe)Si- and MnS-based impurities has been observed in Fig. S4b (Supporting Information) considering Mn takes responsibility for largest magnetic moments in $(Mn,Fe)_2(P,Si)$-based MCMs [67].

Actually, the parent system for $(Mn,Fe)_2(P,Si)$ is the hexagonal Fe_2P metalloid material, for which itinerant ferromagnetism was found to occur based on the Rhodes–Wohlfarth criteria ($q_c/q_s \approx 1.8$) [69–71]. Single crystalline Fe_2P shows a mixture of itinerant and localized magnetism characteristics due to the presence of a strong magnetic anisotropy [72]. This itinerant-electron metamagnet also shows a moment instability for one of the Fe moments, which is similar to $(Mn,Fe)_2(P,Si)$. Also, for $(Mn,Fe)_2(P,Si)$-based MCMs high-resolution synchrotron powder diffraction experiments combined with DFT calculation infer that the metastable moment behavior (Fe moment destabilization) during the phase transition is mainly ascribed to the function of the metalloid atoms (P/Si) [24]. A remarkable electron-density redistribution around Fe atoms was experimentally observed, indicating that this strong magnetoelastic coupling system is dominated by the competition between covalent bonding and ferromagnetic exchange coupling [24]. The chemical coordination environment (like interatomic distances), directly strengthen/weaken the magnetic exchange interactions among various atoms, thereby effectively influencing the electronic configuration around the Fe(3*f*) sites [55].

The Fe-Fe (3*f* intralayer), Mn-Mn (3*g* intralayer), Fe-Mn (3*f*-3*g* interlayer) and Fe-P/Si (3*f* intralayer) atomic distances with different B, C, N, F and S dopant concentrations determined experimen-

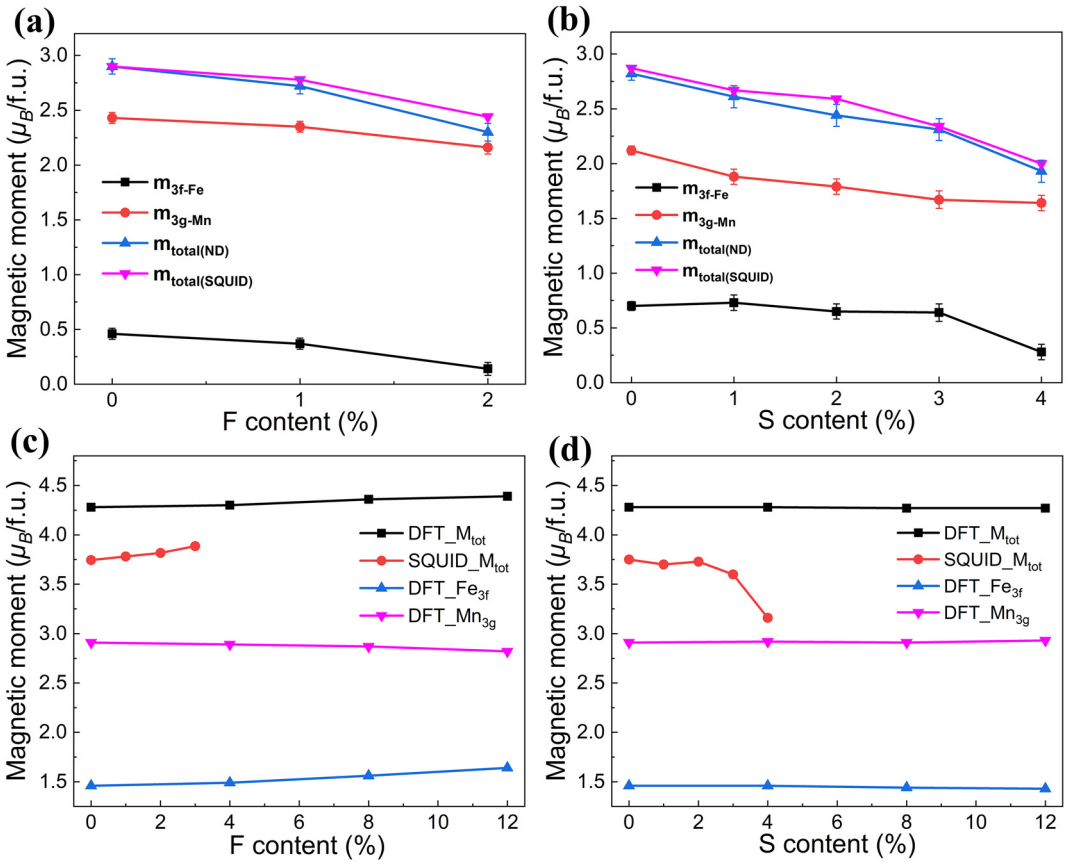

Fig. 7. Experimental magnetic moments obtained from ND and SQUID magnetization measurements at RT for (a) $Mn_{0.60}Fe_{1.30}P_{0.64}Si_{0.36}F_x$ (x = 0.00, 0.01, 0.02) and (b) $Mn_{0.60}Fe_{1.25}P_{0.66\text{-}y}Si_{0.34}S_y$ (y = 0.00, 0.01, 0.02, 0.03, 0.04) alloys. The magnetic moments derived from DFT calculations and magnetization measurements at 5 K as a function of (c) F and (d) S content.

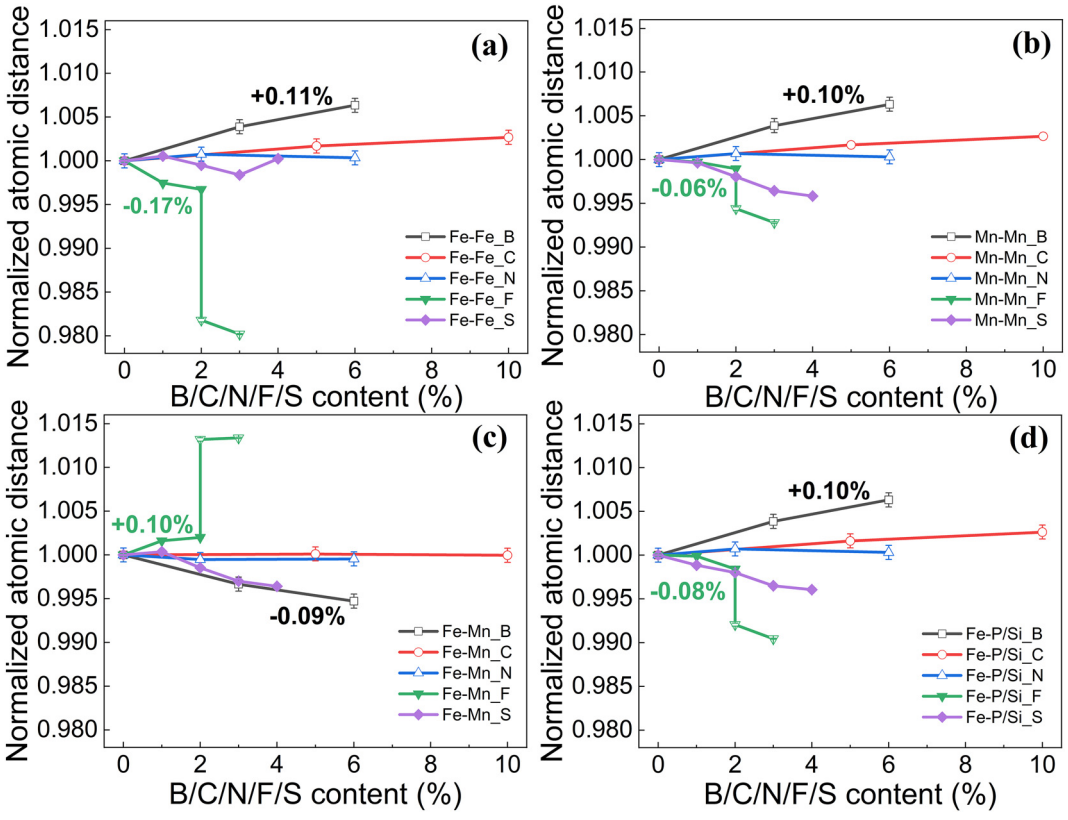

Fig. 8. Normalized interatomic distances of (a) Fe-Fe, (b) Mn-Mn, (c) Fe-Mn and (d) Fe-P/Si as a function of different B, C, N, F and S dopant concentrations for $(Mn,Fe)_2(P,Si)$-based materials, determined from neutron diffraction. Note that the marked normalized atomic distance has been rescaled per dopant concentration (*at.%*).

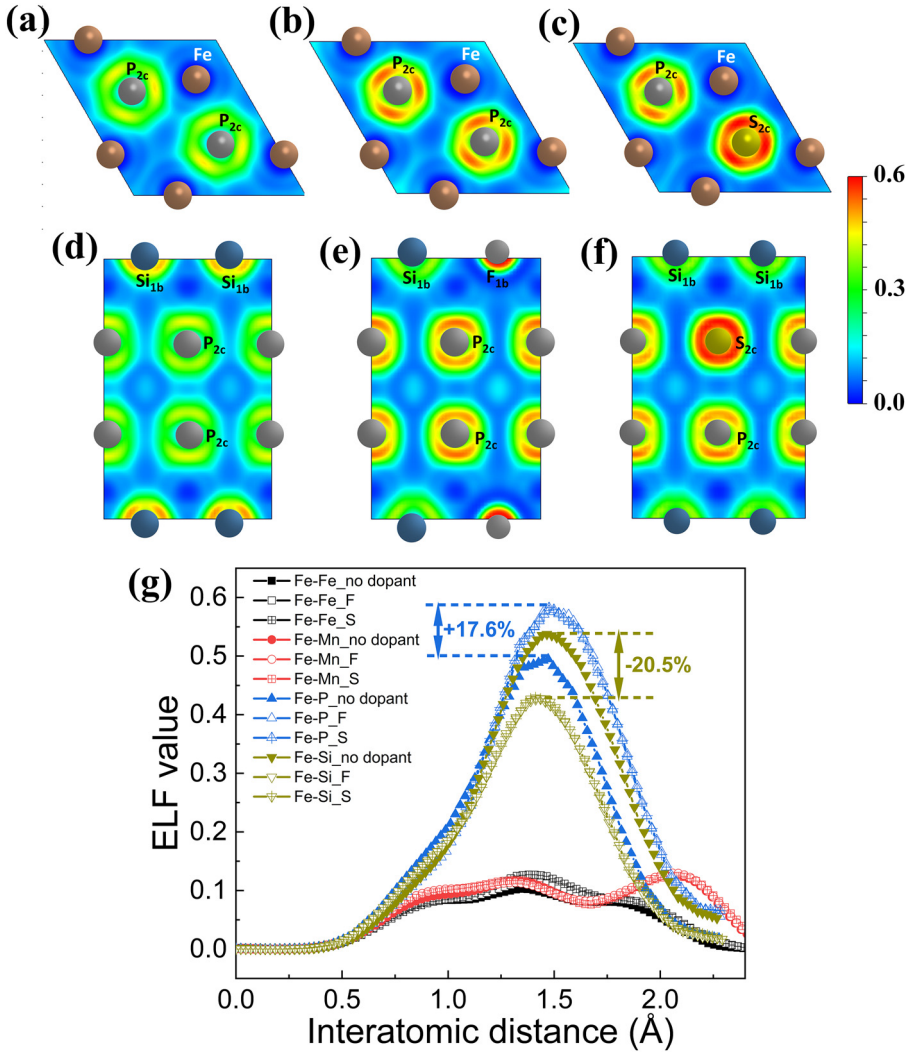

Fig. 9. Calculated ELF contour maps for the *3f* Fe layer with (a) no dopant, (b) F-doping, (c) S-doping sliced along (001) direction and (c) no dopant, (d) F-doping, (e) S-doping sliced along (110) direction in the FM state of the $(Mn,Fe)_2(P,Si)$-based alloys. (g) Line profiles of the ELF values between Fe and its nearest neighbors. The stoichiometry of $MnFeP_{2/3}Si_{1/3}$ is assumed in the supercell for simplicity of the calculations.

tally from ND measurements are shown in Fig. 8(a–d). Note that the P/Si atoms are distributed randomly within 3*g*/3*f* layers. Compared with the isotropic deformations for B doping, the most significant atomic distance change for F dopant is the intralayer Fe(*3f*) - Fe(*3f*) spacing, where the normalized atomic distance changes by −0.17% (per dopant concentration%), as shown in Fig. 8a. This is most likely because the Fe(*3f*) atoms are metastable and the contracted Fe(*3f*) - Fe(*3f*) distance may consolidate the magnetic interaction, whereas the intralayer Mn(3*g*) - Mn(3*g*) distance shows a negligible effect, as shown in Fig. 8b. Meanwhile, recent neutron powder diffraction studies of doping in $(Mn,Fe)_2(P,Ge)$ alloys elucidate that coplanar Fe/Mn–Ge/P bond-length changes have a significant influence on T_C and ΔT_{hys} [73]. Thus, the comparatively small distance changes in the interlayer Fe(*3f*)-metalloid(*2c*) distance (−0.08%) and Fe(*3f*) - Mn(3*g*) distance (+0.10%) together with Fe(*3f*) - Fe(*3f*) distance (-0.17%) for F doping, resulting in a distortion of the tetrahedral Fe(*3f*) site, could contribute to this enhancement in exchange interaction as illustrated in Fig. 8(c,d).

For S doping, the most remarkable change is observed for the intralayer Mn(3*g*)-Mn(3*g*) distance (−0.11%). Based on electronic structure calculations, the Fe/Mn *d* electrons within the $(Mn,Fe)_2(P,Si)$ structure are near the Fermi level, while the P/Si *p* electrons are located far below [55,74]. As a consequence, similar to Si doping [55], free electrons would transfer from the metal *d* band to the metalloid *p* band due to the stronger electronegativity (ability to attract shared electrons) of F ($2s^22p^5$) and S ($3s^23p^4$) atoms, which further enhances the splitting of the *d* band, and therefore increase the magnetic moment. Unfortunately, the introduced impurities suppresses the increased moment potential for S doping.

The Electron Localization Function (ELF), a visualization of the valence shell electron pair repulsion theory, has been applied successfully in intermetallic compounds to distinguish the nature of the chemical covalent/metallic bonding [75–77]. This method is also suitable for the $(Mn,Fe)_2(P,Si)$-based itinerant FM system. In Fig. 9(a–c) and (d–f), the 2D ELF contour plots, sliced along (001) and (110) direction, are shown for (*i*) no dopant, (*ii*) F-doping and (*iii*) S-doping. From the topological analysis of the ELF in Fig. 9(b,c) a significant electron localization around the P(*2c*) atoms is confirmed for F and S doping in comparison with the undoped material (Fig. 9a). This is in agreement with *K*-edge phosphorus X-ray absorption spectroscopy (XAS) results which indicate that P is involved in a charge redistribution [78]. A similar phenomenon is seen in Fig. 9(e,f). Obviously, F/S atoms can effectively promote electron localization around the P(*2c*) atoms, while there is delocalization around the Si(*1b*) atoms. The ELF maps for the Mn

surroundings are shown in Fig. S9 (Supporting Information). The line profiles of the ELF values between the nearest-neighboring atoms are illustrated in Fig. 9g. A higher value (close to maximum 1) means more electron localization. It is noteworthy that the maximum ELF values for nearest Fe-P atoms change from 0.49 to 0.58 (17.6% increase), which indicates a stronger covalent bonding upon F/S doping, while the ELF values for the nearest Fe-Si atoms decrease from 0.54 to 0.43 (20.5% decrease). These covalent bonding properties for F/S doped systems are essentially associated with the charge transfer from the *p-d* covalent hybridization. The combined atomic distance changes jointly contribute to the total moments enhancement for the F-doped $(Mn,Fe)_2(P,Si)$ system and help to stabilize the hexagonal phase. Taking metalloids as the entry point, our current study on introducing non-metal species provide a new way to further optimize the MCE performance by regulating the metastability in bonding and atomic distances.

5. Conclusions

In summary, the light elements F and S have successfully been introduced into $(Mn,Fe)_2(P,Si)$-based MCMs and the thermodynamic and magnetic properties of the new materials synthesised have been investigated. For these two dopant systems T_C can be moved sufficiently into the RT range. Interestingly, it is found that F doping enhances the magnetocaloric effect at the FOMT (by an increase in magnetic moments and in $|\Delta S_m|$), while for S doping the generated impurities slowly weaken the FOMT. By performing ND experiments the site occupancy has been resolved, indicating that F and S are substituted on the *1b* and *2c* site, respectively. This site preference has been confirmed by DFT calculations. The tunable MCE properties with F/S doping are analyzed in terms of the experimental atomic distances among different metal-metal or metal-metalloids atom pairs. Together with theoretical ELF calculations, these results clarify the subtle atomic distance changes, as well as the covalent bonding. Together they determine the change in GMCE with doping in these magnetoelastic $(Mn,Fe)_2(P,Si)$-based materials. Our results provide important insights and systematic understanding into the effect of doping with light elements on the GMCE properties of $(Mn,Fe)_2(P,Si)$-based MCMs.

Declaration of Competing Interest

The authors declare that they have no known competing financial interests or personal relationships that could have appeared to influence the work reported in this paper.

Acknowledgments

The authors thank Anton Lefering, Bert Zwart, Robert Dankelman and Michel Steenvoorden for their technical assistance. This work was supported by NWO in the domain of the Applied and Engineering Sciences (AES) program. Fengqi Zhang gratefully acknowledges financial support from the China Scholarship Council, and specially thanks to Dr. Xuefei Miao for providing original ND data about B-, C-, N-doped $(Mn,Fe)_2(P,Si)$ works. Data collection on Polaris at the ISIS Pulsed Neutron and Muon Source was supported by an Xpress Access beam time allocation from the Science and Technology Facilities Council (proposals XB2090003-2090006 and XB2090080-2090084)

Supplementary materials

Supplementary material associated with this article can be found, in the online version, at doi:10.1016/j.actamat.2022.118057.

References

[1] A. Kitanovski, Energy applications of magnetocaloric materials, Adv. Energy Mater. 10 (2020) 1903741.
[2] H. Johra, K. Filonenko, P. Heiselberg, C. Veje, S. Dall'Olio, K. Engelbrecht, C. Bahl, Integration of a magnetocaloric heat pump in an energy flexible residential building, Renew. Energy 136 (2019) 115–126.
[3] A. Waske, D. Dzekan, K. Sellschopp, D. Berger, A. Stork, K. Nielsch, S. Fahler, Energy harvesting near room temperature using a thermomagnetic generator with a pretzel-like magnetic flux topology, Nat Energy 4 (2019) 68–74.
[4] D. Dzekan, A. Waske, K. Nielsch, S. Fahler, Efficient and affordable thermomagnetic materials for harvesting low grade waste heat, APL Mater. 9 (2021) 011105.
[5] V.K. Pecharsky, K.A. Gschneidner, Giant magnetocaloric effect in $Gd_5(Si_2Ge_2)$, Phys. Rev. Lett. 78 (1997) 4494–4497.
[6] O. Tegus, E. Brück, K.H.J. Buschow, F.R. de Boer, Transition-metal-based magnetic refrigerants for room-temperature applications, Nature 415 (2002) 150–152.
[7] F.X. Hu, B.G. Shen, J.R. Sun, Z.H. Cheng, G.H. Rao, X.X. Zhang, Influence of negative lattice expansion and metamagnetic transition on magnetic entropy change in the compound $LaFe_{11.4}Si_{1.6}$, Appl. Phys. Lett. 78 (2001) 3675–3677.
[8] A. Planes, L. Manosa, M. Acet, Magnetocaloric effect and its relation to shape-memory properties in ferromagnetic Heusler alloys, J. Phys. Condens. Mater. 21 (2009) 233201.
[9] A. Chirkova, K.P. Skokov, L. Schultz, N.V. Baranov, O. Gutfleisch, T.G. Woodcock, Giant adiabatic temperature change in FeRh alloys evidenced by direct measurements under cyclic conditions, Acta Mater. 106 (2016) 15–21.
[10] P.A.E. Murgatroyd, K. Routledge, S. Durdy, M.W. Gaultois, T.W. Surta, M.S. Dyer, J.B. Claridge, S.N. Savvin, D. Pelloquin, S. Hebert, J. Alaria, Chemically controllable magnetic transition temperature and magneto-elastic coupling in MnZnSb compounds, Adv. Funct. Mater. 31 (2021) 2100108.
[11] J. Liu, Y.Y. Gong, Y.R. You, X.M. You, B.W. Huang, X.F. Miao, G.Z. Xu, F. Xu, E. Brück, Giant reversible magnetocaloric effect in MnNiGe-based materials: minimizing thermal hysteresis via crystallographic compatibility modulation, Acta Mater. 174 (2019) 450–458.
[12] L. Caron, N.T. Trung, E. Brück, Pressure-tuned magnetocaloric effect in $Mn_{0.93}Cr_{0.07}CoGe$, Phys. Rev. B 84 (2011) 020414.
[13] L. Manosa, A. Planes, Solid-state cooling by stress: a perspective, Appl. Phys. Lett. 116 (2020) 050501.
[14] V. Paul-Boncour, L. Bessais, Tuning the magnetocaloric properties of the $La(Fe,Si)_{13}$ compounds by chemical substitution and light element insertion, Magnetochemistry 7 (2021) 1–18.
[15] M.M. Cicek, S. Saritas, O. Yildirim, B. Emre, Effect of the low constituent boron on martensitic transformation, magnetic, and magnetocaloric properties of $Ni_{50}Mn_{35}In_{15}$ Heusler alloys, J. Alloy. Compd. 845 (2020) 155493.
[16] H.Z. Luo, F.B. Meng, Q.X. Jiang, H.Y. Liu, E.K. Liu, G.H. Wu, Y.X. Wang, Effect of boron on the martensitic transformation and magnetic properties of $Ni_{50}Mn_{36.5}Sb_{13.5-x}B_x$ alloys, Scr. Mater. 63 (2010) 569–572.
[17] S. Kavita, V.V. Ramakrishna, P. Yadav, S. Kethavath, N.P. Lalla, T. Thomas, P. Bhatt, R. Gopalan, Enhancement of martensite transition temperature and inverse magnetocaloric effect in $Ni_{43}Mn_{47}Sn_{11}$ alloy with B doping, J. Alloy. Compd. 795 (2019) 519–527.
[18] Y. Zhang, J. Liu, Q. Zheng, J. Zhang, W.X. Xia, J. Du, A.R. Yan, Large magnetic entropy change and enhanced mechanical properties of Ni-Mn-Sn-C alloys, Scr. Mater. 75 (2014) 26–29.
[19] F. Guillou, G. Porcari, H. Yibole, N. van Dijk, E. Brück, Taming the first-order transition in giant magnetocaloric materials, Adv. Mater. 26 (2014) 2671–2675.
[20] J.W. Lai, B.W. Huang, X.F. Miao, N.V. Thang, X.M. You, M. Maschek, L. van Eijck, D.C. Zeng, N. van Dijk, E. Brück, Combined effect of annealing temperature and vanadium substitution for mangetocaloric $Mn_{1.2-x}V_xFe_{0.75}P_{0.5}Si_{0.5}$ alloys, J. Alloy. Compd. 803 (2019) 671–677.
[21] J.T. Feng, F.J. Qian, D.N. Shi, H. Yang, Effect of Zr substitution on the crystal structure, magnetoelastic transition and magnetocaloric properties of $(Mn,Fe)_2(P,Si)$ alloys, Appl. Phys. 9 (2019) 358–364.
[22] S.Y. Hu, X.F. Miao, J. Liu, Z.Q. Ou, M.Q. Cong, O. Haschuluu, Y.Y. Gong, F.J. Qian, Y.R. You, Y.J. Zhang, F. Xu, E. Bruck, Small hysteresis and giant magnetocaloric effect in Nb-substituted $(Mn,Fe)_2(P,Si)$ alloys, Intermetallics 114 (2019) 106602.
[23] X.F. Miao, Y. Gong, F.Q. Zhang, Y.R. You, L. Caron, F.J. Qian, W.H. Guo, Y.J. Zhang, Y.Y. Gong, F. Xu, N.H. van Dijk, E. Brück, Enhanced reversibility of the magnetoelastic transition in $(Mn,Fe)_2(P,Si)$ alloys via minimizing the transition-induced elastic strain energy, J. Mater. Sci. Technol. 103 (2022) 165–176.
[24] M.F.J. Boeije, P. Roy, F. Guillou, H. Yibole, X.F. Miao, L. Caron, D. Banerjee, N.H. van Dijk, R.A. de Groot, E. Brück, Efficient room-temperature cooling with magnets, Chem. Mater. 28 (2016) 4901–4905.
[25] W. Gordy, W.J.O. Thomas, Electronegativities of the elements, J. Chem. Phys. 24 (1956) 439–444.
[26] L. Pauling, The nature of the chemical bond. IV. The energy of single bonds and the relative electronegativity of atoms, J. Am. Chem. Soc. 54 (1932) 3570–3582.
[27] K.Y. Li, D.F. Xue, Estimation of electronegativity values of elements in different valence states, J. Phys. Chem. A 110 (2006) 11332–11337.
[28] B. Cordero, V. Gomez, A.E. Platero-Prats, M. Reves, J. Echeverria, E. Cremades, F. Barragan, S. Alvarez, Covalent radii revisited, Dalton Trans. 21 (2008) 2832–2838.
[29] X.F. Miao, L. Caron, Z. Gercsi, A. Daoud-Aladine, N.H. van Dijk, E. Brück, Thermal-history dependent magnetoelastic transition in $(Mn,Fe)_2(P,Si)$, Appl. Phys. Lett. 107 (2015) 042403.

[30] N.H. Dung, Moment Formation and Giant Magnetocaloric Effects in Hexagonal Mn-Fe-P-Si Compounds, TU Delft, 2012 PhD Thesis.

[31] G. Porcari, F. Cugini, S. Fabbrici, C. Pernechele, F. Albertini, M. Buzzi, M. Mangia, M. Solzi, Convergence of direct and indirect methods in the magnetocaloric study of first order transformations: the case of Ni-Co-Mn-Ga Heusler alloys, Phys. Rev. B 86 (2012) 104432.

[32] R.I. Smith, S. Hull, M.G. Tucker, H.Y. Playford, D.J. McPhail, S.P. Waller, S.T. Norberg, The upgraded Polaris powder diffractometer at the ISIS neutron source, Rev. Sci. Instrum. 90 (2019) 115101.

[33] N.H. van Dijk, Resolving the site occupancy of nonmetal atoms in $(Mn,Fe)_2(P,Si,F/S)$ magnetocaloric compounds, STFC ISIS Neutron Muon Source (2020), doi:10.5286/ISIS.E.RB2090003-1. https://doi.org/10.5286/ISIS.E.RB2090004-1, https://doi.org/10.5286/ISIS.E.RB2090005-1, https://doi.org/10.5286/ISIS.E.RB2090006-1, https://doi.org/10.5286/ISIS.E.RB20900080-1, https://doi.org/10.5286/ISIS.E.RB20900081-1, https://doi.org/10.5286/ISIS.E.RB20900082-1, https://doi.org/10.5286/ISIS.E.RB20900083-1, https://doi.org/10.5286/ISIS.E.RB20900084-1.

[34] H.M. Rietveld, A profile refinement method for nuclear and magnetic structures, J. Appl. Crystallogr. 2 (1969) 65–71.

[35] G. Kresse, J. Hafner, Ab initio molecular dynamics for liquid metals, Phys. Rev. B 47 (1993) 558–561.

[36] G. Kresse, J. Furthmuller, Efficiency of ab-initio total energy calculations for metals and semiconductors using a plane-wave basis set, Comput. Mater. Sci. 6 (1996) 15–50.

[37] P.E. Blochl, Projector augmented-wave method, Phys. Rev. B 50 (1994) 17953–17979.

[38] G. Kresse, D. Joubert, From ultrasoft pseudopotentials to the projector augmented-wave method, Phys. Rev. B 59 (1999) 1758–1775.

[39] J.P. Perdew, K. Burke, M. Ernzerhof, Generalized gradient approximation made simple, Phys. Rev. Lett. 77 (1996) 3865–3868.

[40] D.I. Bolef, N.T. Melamed, M. Menes, Elastic constants of hexagonal cadmium sulfide, J. Phys. Chem. Solids 17 (1960) 143–148.

[41] L. Fast, J.M. Wills, B. Johansson, O. Eriksson, Elastic-constants of hexagonal transition-metals-theory, Phys. Rev. B 51 (1995) 17431–17438.

[42] P. Roy, E. Torun, R.A. de Groot, Effect of doping and elastic properties in $(Mn,Fe)_2(Si,P)$, Phys. Rev. B 93 (2016) 094110.

[43] M. Methfessel, A.T. Paxton, High-precision sampling for Brillouin-zone integration in metals, Phys. Rev. B 40 (1989) 3616–3621.

[44] B. Silvi, A. Savin, Classification of chemical-bonds based on topological analysis of electron localization functions, Nature 371 (1994) 683–686.

[45] P. Roy, E. Brück, R.A. de Groot, Latent heat of the first-order magnetic transition of $MnFeSi_{0.33}P_{0.66}$, Phys. Rev. B 93 (2016) 165101.

[46] T. Gottschall, K.P. Skokov, M. Fries, A. Taubel, I. Radulov, F. Scheibel, D. Benke, S. Riegg, O. Gutfleisch, Making a cool choice: the materials library of magnetic refrigeration, Adv. Energy Mater. 9 (2019) 1901322.

[47] J. Lyubina, Magnetocaloric materials for energy efficient cooling, J. Phys. D Appl. Phys. 50 (2017) 053002.

[48] J.W. Lai, Z.G. Zheng, B.W. Huang, H.Y. Yu, Z.G. Qiu, Y.L. Mao, S. Zhang, F.M. Xiao, D.C. Zeng, K. Goubitz, E. Brück, Microstructure formation and magnetocaloric effect of the Fe_2P-type phase in $(Mn,Fe)_2(P,Si,B)$ alloys, J. Alloy. Compd. 735 (2018) 2567–2573.

[49] V. Johnson, D.B. Rogers, J.F. Weiher, C.G. Frederick, Magnetic and mössbauer–effect studies of Mn_5Si_3:Fe_5Si_3 solid-solutions, J. Solid State Chem. 4 (1972) 311–323.

[50] V. Singh, P. Bag, R. Rawat, R. Nath, Critical behavior and magnetocaloric effect across the magnetic transition in $Mn_{1+x}Fe_{4-x}Si_3$, Sci. Rep. 10 (2020) 6981 UK.

[51] Z. Gercsi, E.K. Delczeg-Czirjak, L. Vitos, A.S. Wills, A. Daoud-Aladine, K.G. Sandeman, Magnetoelastic effects in doped Fe_2P, Phys. Rev. B 88 (2013) 024417.

[52] X.F. Miao, N.V. Thang, L. Caron, H. Yibole, R.I. Smith, N.H. van Dijk, E. Brück, Tuning the magnetoelastic transition in $(Mn,Fe)_2(P,Si)$ by B, C, and N doping, Scr. Mater. 124 (2016) 129–132.

[53] X.F. Miao, L. Caron, J. Cedervall, P.C.M. Gubbens, P.D. de Reotier, A. Yaouanc, F. Qian, A.R. Wildes, H. Luetkens, A. Amato, N.H. van Dijk, E. Brück, Short-range magnetic correlations and spin dynamics in the paramagnetic regime of $(Mn,Fe)_2(P,Si)$, Phys. Rev. B 94 (2016) 014426.

[54] X.F. Miao, Y. Mitsui, A.I. Dugulan, L. Caron, N.V. Thang, P. Manuel, K. Koyama, K. Takahashi, N.H. van Dijk, E. Brück, Kinetic-arrest-induced phase coexistence and metastability in $(Mn,Fe)_2(P,Si)$, Phys. Rev. B 94 (2016) 094426.

[55] X.F. Miao, L. Caron, P. Roy, N.H. Dung, L. Zhang, W.A. Kockelmann, R.A. de Groot, N.H. van Dijk, E. Brück, Tuning the phase transition in transition-metal-based magnetocaloric compounds, Phys. Rev. B 89 (2014) 174429.

[56] D. Scheerlinck, E. Legrand, Neutron diffraction study of the magnetic structure of Fe_2P, Solid State Commun. 25 (1978) 181–184.

[57] J. Cedervall, M.S. Andersson, E.K. Delczeg-Czirjak, D. Iusan, M. Pereiro, P. Roy, T. Ericsson, L. Haggstrom, W. Lohstroh, H. Mutka, M. Sahlberg, P. Nordblad, P.P. Deen, Magnetocaloric effect in Fe_2P: magnetic and phonon degrees of freedom, Phys. Rev. B 99 (2019) 174437.

[58] E.K. Delczeg-Czirjak, Z. Gercsi, L. Bergqvist, O. Eriksson, L. Szunyogh, P. Nordblad, B. Johansson, L. Vitos, Magnetic exchange interactions in B-, Si-, and As–doped Fe_2P from first-principles theory, Phys. Rev. B 85 (2012) 224435.

[59] L.F. Cohen, Contributions to hysteresis in magnetocaloric materials, Phys. Status Solidi B 255 (2018) 1700317.

[60] J. Liu, X.M. You, B.W. Huang, I. Batashev, M. Maschek, Y.Y. Gong, X.F. Miao, F. Xu, N. van Dijk, E. Brück, Reversible low-field magnetocaloric effect in Ni-Mn-In-based Heusler alloys, Phys. Rev. Mater. 3 (2019) 084409.

[61] J.W. Lai, H. Sepehri-Amin, X. Tang, J. Li, Y. Matsushita, T. Ohkubo, A.T. Saito, K. Hono, Reduction of hysteresis in $(La_{1-x}Ce_x)_y(Mn_zFe_{11.4-z})Si_{1.6}$ magnetocaloric compounds for cryogenic magnetic refrigeration, Acta Mater. 220 (2021) 117286.

[62] M.F.J. Boeije, M. Maschek, X.F. Miao, N.V. Thang, N.H. van Dijk, E. Brück, Mixed magnetism in magnetocaloric materials with first-order and second-order magnetoelastic transitions, J. Phys. D Appl. Phys. 50 (2017) 174002.

[63] G.F. Cardinale, D.L. Medlin, P.B. Mirkarimi, K.F. McCarty, D.G. Howitt, Orientation-dependence of elastic strain energy in hexagonal and cubic boron nitride layers in energetically deposited BN films, J. Vac. Sci. Technol. A 15 (1997) 196–200.

[64] J.Y. Shen, S. Johnston, S.L. Shang, T. Anderson, Calculated strain energy of hexagonal epitaxial thin films, J. Cryst. Growth 240 (2002) 6–13.

[65] J.F. Nye, Physical Properties of Crystals: Their Representation by Tensors and Matrices, Oxford University Press, 1985.

[66] B.K. Banerjee, On a generalised approach to first and second order magnetic transitions, Phys. Lett. 12 (1964) 16–17.

[67] N.H. Dung, Z.Q. Ou, L. Caron, L. Zhang, D.T.C. Thanh, G.A. de Wijs, R.A. de Groot, K.H.J. Buschow, E. Brück, Mixed magnetism for refrigeration and energy conversion, Adv. Energy Mater. 1 (2011) 1215–1219.

[68] M. Maschek, X. You, M.F.J. Boeije, D. Chernyshov, N.H. van Dijk, E. Brück, Charge redistribution and the magnetoelastic transition across the first-order magnetic transition in $(Mn,Fe)_2(P,Si,B)$, Phys. Rev. B 98 (2018) 224413.

[69] S. Kumar, A. Krishnamurthy, B.K. Srivastava, On nature of magnetism in ferromagnetic alloys $(Fe_{1-x}Co_x)_2P$, J. Phys. D Appl. Phys. 41 (2008) 055001.

[70] O. Eriksson, J. Sjostrom, B. Johansson, L. Haggstrom, H.L. Skriver, Itinerant ferromagnetism in Fe_2P, J. Magn. Magn. Mater. 74 (1988) 347–358.

[71] E.P. Wohlfarth, Magnetic properties of crystallineand amorphous alloys: a systematic discussion based on the Rhodes-Wohlfarth plot, J. Magn. Magn. Mater. 7 (1978) 113–120.

[72] L. Caron, M. Hudl, V. Hoglin, N.H. Dung, C.P. Gomez, M. Sahlberg, E. Brück, Y. Andersson, P. Nordblad, Magnetocrystalline anisotropy and the magnetocaloric effect in Fe_2P, Phys. Rev. B 88 (2013) 094440.

[73] H.R. Zhang, D.M. Liu, Z.L. Zhang, S.B. Wang, M. Yue, Q.Z. Huang, J.W. Lynn, The correlation between the covalent bonds and magnetocaloric properties of the $Mn_{2-x}Fe_xP_yGe_{1-y}M_z$ compounds, J. Appl. Phys. 130 (2021) 133901.

[74] P. Jernberg, A.A. Yousif, L. Häggström, Y. Andersson, A Mössbauer study of $Fe_2P_{1-x}Si_x$ ($x \leq 0.35$), J. Solid State Chem. 53 (1984) 313–322.

[75] A.D. Becke, K.E. Edgecombe, A simple measure of electron localization in atomic and molecular-systems, J. Chem. Phys. 92 (1990) 5397–5403.

[76] A. Savin, R. Nesper, S. Wengert, T.F. Fassler, ELF: the electron localization function, Angew. Chem. Int. Ed. 36 (1997) 1809–1832.

[77] E.K. Liu, W.H. Wang, L. Feng, W. Zhu, G.J. Li, J.L. Chen, H.W. Zhang, G.H. Wu, C.B. Jiang, H.B. Xu, F. de Boer, Stable magnetostructural coupling with tunable magnetoresponsive effects in hexagonal ferromagnets, Nat. Commun. 3 (2012) 873.

[78] F. Guillou, K. Ollefs, F. Wilhelm, A. Rogalev, A.N. Yaresko, H. Yibole, N.H. van Dijk, E. Brück, Electronic and magnetic properties of phosphorus across the first-order ferromagnetic transition of $(Mn,Fe)_2(P,Si,B)$ giant magnetocaloric materials, Phys. Rev. B 92 (2015) 224427.